INFLUENCE OF FREE - PLAY AND FRICTION IN CONTROL SYSTEM ON AIRCRAFT FLIGHT DYNAMICS

Krzysztof Sibilski*, Jozef Zurek*, Wieslaw Wroblewski**
***Air Force Institute of Technology, ****Wroclaw University of Technology**

Keywords: *nonlinear flight dynamics, dynamical systems theory, bifurcation theory*

Abstract

The Faults such as actuator failures in aircraft result in significant deviation from the nominal dynamics and may cause departure in to highly nonlinear regimes. In this work introduce: the models of friction in kinematics' peers of control system, the model of free – play models, as well as the model of servomechanisms dynamics, regarding the limitations putting on movement of individual executive units of arrangement of control system. We use continuation methods to identify bifurcation points of the fighter aircraft model for the nominal system and various single actuator failure situations.

1 Introduction

The Faults such as actuator failures in aircraft result in significant deviation from the nominal dynamics and may cause departure in to highly nonlinear regimes. There is need for the development of relevant nonlinear analysis and simulation tools to aid the design and verification of reconfigured control laws. Since the impaired aircraft operate with a restricted maneuverability envelope relative to fully functional vehicles it is necessary to be able to evaluate post failure flight control system performance. Understanding the behavior near operational limits and developing control and recovery strategies for these circumstances is fundamental to achieving flight safety goals.
The problem of flight control reconfiguration following actuator failure has been formulated as a nonlinear regulator problem (see for example refs. [1, 2]). The post-fault controller uses the remaining functional actuators. It is designed to regulate key flight parameters while rejecting the disturbance induced by the failed actuator. The idea is that the pilot would maneuver the impaired aircraft by specifying the desired flight parameters. The post fault system dynamics can differ significantly from normal conditions, and the aircraft can be expected to operate within limited stability boundaries. The ability of the impaired aircraft to maneuver needs to bee valuated. This can be accomplished by analyzing the aircraft equilibrium point structure.
Using a continuation method the equilibrium surface is generated by varying a single parameter such as airspeed or flight path angle. Thus, a co-dimension one surface is obtained in the space of states and (functional) controls. On this surface we identify:

1. points at which stability is lost,
2. functional actuator limits,
3. static bifurcation points.

The most binding of these identify the limits of variability associated with the continuation parameter. Thus, we can identify the maneuverability envelope associated with any failure.

2 The Continuation and Bifurcation Approach

2.1 Bifurcation-based analysis technique

Bifurcation analysis essentially finds solutions (or "continues") along surfaces of solutions expressed as a function of a state vector x and a continuation parameter vector μ. In aircraft problems $\mathbf{x}$ is a vector of aircraft states and μ is a vector of control inputs. The solution surfaces

are typically folded, i.e. they bifurcate, and hence difficult to continue along. The power of Bifurcation Analysis lies in its ability to systematically search for these bifurcating solution surfaces. Nonlinear Bifurcation methods were originally developed and applied for departure prediction and spin analysis [5-10]. Bifurcation Analysis principally provides a picture of the globally attainable steady state equilibrium conditions by a platform with a given set of control powers. "Equilibrium" is used here in the global sense, i.e. straight and level flight as well as limit cycle oscillations such as wing rock regimes or oscillatory spins. The technique is smart in that, once it finds an initial trim solution, it generates the entire set of equilibrium solutions (or "branch" of solutions) on a continuous solution space very rapidly and without significant user intervention.

The methods are well suited to the analysis of highly non-linear regions of the flight envelope where significant aerodynamic and inertial or kinematic coupling is exhibited due to vortex flow breakdown. This coupling typically manifests as spin and other undesired modes that are unique a particular air plat-form and that must be avoided by careful design of the stabilizing flight control system. Bifurcation Analysis provides an understanding of the basic airframe characteristics and underlying causes of instability and uncontrollability. It enables classification of "safe" and "unsafe" regions of the flight envelope and accurate pinpointing of control critical flight conditions, e.g. where there may be insufficient control powers for departure recovery.

The methodology is founded upon the use of "continuation methods", which are a fundamental tool in numerical bifurcation analysis. Bifurcation analysis is a process used to study the behavior of non-linear dynamical systems in terms of the geometry of their underlying structure, as characterized by the evolution of steady state solutions as parameters vary. Steady states include in general stationary point equilibria and periodic orbits (and other attractors) and non-linear systems can have multiple steady states for the same values of input parameters.

One means of visualizing the numerical output is the "one-parameter bifurcation diagram": projections of the steady state solution paths as a parameter varies, plotted as one state component at a time versus the parameter. The algorithms used to generate this information are known as "continuation methods" - and it is principally this that is adapted to form the bifurcation-based analysis technique.

Given a non-linear dynamical system, $\dot{\mathbf{x}} = \mathbf{f}(\mathbf{x}, \boldsymbol{\mu})$, where $\mathbf{x}$ is the state vector, $\boldsymbol{\mu}$ is a vector of parameters and $\mathbf{f}$ is a smooth vector function, we choose one member of $\boldsymbol{\mu}$ as the parameter to vary (the continuation parameter, λ) and fix the remaining components of $\boldsymbol{\mu}$. For equilibria steady states (the only type considered in this paper), we then solve for $\dot{\mathbf{x}} = \mathbf{f}(\mathbf{x}, \lambda) = 0$ as λ varies; the idea is to find all solutions within the required range of λ. The continuation method is thus a path-following algorithm which, given a starting guess, attempts to continue along the solution branch. Bifurcation points are identified along the path and often it is required to solve also for the new solution branches that arise from them. Usually, local stability along the branches is indicated by use of different line types on the bifurcation diagrams; bifurcation points are also indicated where necessary.

When applied to aircraft flight dynamics models the parameters are usually the inputs to the system (control surfaces or pilot demands). However, for the purposes of control law clearance analysis, the parameters include uncertainty parameters and model variabilities. The process of applying continuation methods to clearance analysis involves generating the steady state solution branch, as in standard bifurcation analysis. The model used is set up to represent whatever form of 'trim' is specified for the clearance task.

Once each solution point is found, one or more clearance criteria is evaluated at that point. The criteria may use a different form of the model, such as with controller command path omitted or with an actuator loop cut, to match the clearance requirement. Thus the versatility of continuation methods is exploited in the process: using one form of model for finding the

steady state solution and one or more others for application of criteria at each solution (this is referred to as the 'dual-model' continuation framework). Note that the criteria are implemented as in a conventional baseline clearance process, so there is no conservatism involved. The "bifurcation diagrams" generated during the analysis may adopt line-type definitions corresponding to the outcome of a clearance criterion.

A detailed description of the analysis cycle is given in ref. [10, 11]. In principle, the process is as follows: first, for each FC, evaluate each clearance criterion along the required trim points across the specified α range for the nominal model (no uncertainties applied). This involves a continuation run, with an appropriate pilot input as continuation parameter; it shows α's where the nominal system violates the criteria, or values where it comes closest to doing so. These points may be referred to as nominal critical points and suggest where the system should be studied further (it is this logic that provides the majority of time saving relative to the conventional gridded approach[1]).

The next step is to evaluate each criterion in the neighborhoods of each critical nominal point, with uncertainties applied. The continuation method is now run at each such point, with α fixed, and the uncertainty parameters used as continuation parameter, one at a time. In the first iteration, the remaining uncertainties are fixed at their nominal value. Each of these non-linear sensitivity bifurcation diagrams indicates the change in clearance criterion as the variable uncertainty ranges from its minimum to maximum value; it reveals the value of this uncertainty that gives the worst case (biggest degradation in criterion measure) while the others are fixed at their nominal value. We repeat this step of varying one uncertainty at a time but now the others take on their worst-case value from the first iteration. This approach allows the worst-case value of each uncertainty to lie anywhere between its minimum and maximum values, but we follow the conventional clearance process and choose either the minimum or the maximum value. Iterations continue until there is no change relative to the previous iteration.

This yields the worst-case combination of uncertainties for that specific solution point for the criterion under consideration. Furthermore, since it gives a quantitative change in criterion measure for each uncertainty, it is possible to invoke the reduction factors for aerodynamic uncertainties. This allows the choice of all the uncertainties to be compared with a selection of a subset of the uncertainties - something that the conventional baseline method does not do.

Finally, a continuation run with the pilot input as continuation parameter is conducted again but this time using the worst-case combination of uncertainties. This identifies the α at which the system violates the criterion under worst-case conditions. It is only strictly applicable in the local neighborhood of the nominal critical point because the worst-case combination was determined at that specific α. This is repeated in the region of each nominal critical point for each criterion at each flight condition, giving the desired cleared and uncleared α regions.

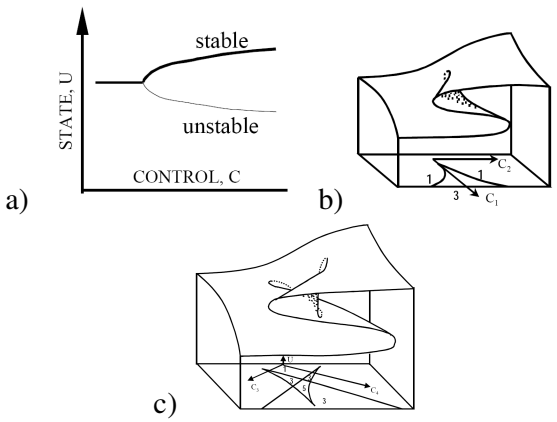

Fig. 1 Different equilibrium structures: a) Fold; b) Cusp c) Butterfly

Generally speaking, bifurcation analysis is the study of the global behavior of nonlinear systems in an $(n+m)$ dimensional space where n is the number of state variables and m is the number of control variables in the system.

[1] Violation of a criterion with uncertainties applied at an α far from the nominal critical points is not likely unless there is a discontinuity in the system - e.g. a non-smooth mode change - that occurs when uncertainties are applied but not in the nominal case. Such situations can be missed also in the conventional gridding method

The bifurcation surfaces are the projection of the equilibrium surfaces (n) onto the control space (m). A bifurcation surface divides regions in the control space where different numbers of equilibrium states are possible. As examples, Fig. 1 show scenarios of bifurcation structures with one state variable and a one or two control variable space corresponding to Fold, Cusp and Butterfly respectively. As controls vary in such a way as to cross the bifurcation surface, catastrophes in the form of sudden "jumps" between equilibrium solutions occur. The solution is said to bifurcate to a new equilibrium branch in state space. The bifurcation surface marks the boundary between the stable and unstable equilibrium solutions. Hysteresis effects may be prevalent where bifurcations occur. The above facts raise the possibility that control recovery actions, which are effective in stable and/or linear regions of the equilibrium state space, may be ineffective or actually counterproductive, once a bifurcation has occurred.

2.2 The mathematical model of aircraft and control system dynamics

Non-linear equations of aircraft motion and the kinematic relations will be expressed by using moving co-ordinate systems, the common origin of which is located at the aircraft center of mass (Fig. 2). In our approach we include mechanical model of control system. As example could be kinematic scheme of longitudinal control system of the fighter aircraft (Fig. 3).

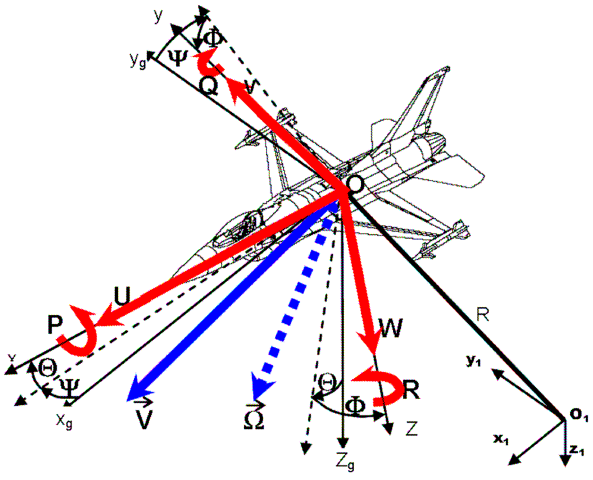

Fig. 2 System of co-ordinates attached to the aircraft

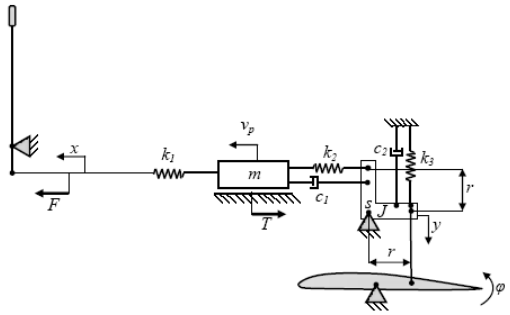

Fig. 3 The kinematic scheme of longitudinal control system [28]

The formalism of analytical mechanics allows to present dynamic equations of motion of mechanical systems in quasi-coordinates, giving incredibly interesting and comfortable tool for construction of equation of motion of aircraft. An example can be Boltzman-Hamel equations, which are generalization of Lagrange equations of the second kind for quasi-coordinates. Boltzmann-Hamel equations have the following form [9]:

$$\frac{d}{dt}\left(\frac{\partial T^*}{\partial \omega_\sigma}\right)-\frac{\partial T^*}{\partial \pi_\sigma}+\sum_{\mu=1}^{k}\sum_{\lambda=1}^{k}\gamma_{\sigma\lambda}^{\mu}\frac{\partial T^*}{\partial \omega_\mu}\omega_\lambda=Q_\sigma^* \qquad (1)$$

where:

T^* – kinetic energy (function of quasi-coordinates and quasi-velocities),

ω_σ – quasi-velocity,

π_σ – quasi-coordinate,

q_λ, q_σ – generaized coordinates,

$Q_\sigma^*=\sum_{\sigma=1}^{k} Q_\sigma b_{\sigma\mu}$ – a coordinates of generalized force vector,

k – number of degree of freedom of mechanical system,

$\gamma_{\mu\alpha}^{r}$ are the Boltzmann symbols [9],

$$\gamma_{\mu\alpha}^{r}=\sum_{r=1}^{k}\sum_{\alpha=1}^{k}\left(\frac{\partial a_{r\sigma}}{\partial q_\lambda}-\frac{\partial a_{r\lambda}}{\partial q_\sigma}\right)b_{\sigma\mu}b_{\lambda\alpha} \qquad (2)$$

and $a_{r\sigma}, b_{r\sigma}$ are elements of transformation matrix. Relations between quasi-velocities and generalized velocities are shown in equations are following:

$$\omega_\sigma=\sum_{\alpha=1}^{k}a_{\sigma\alpha}(q_1,q_2,..,q_k)\cdot\dot{q}_\alpha,$$
$$\dot{q}_\sigma=\sum_{m=1}^{k}b_{\sigma\mu}(q_1,q_2,..,q_k)\cdot\omega_\mu,\ \sigma=1,...,k \qquad (3)$$

Esq. (4) can be written in the matrix form:

$$\mathbf{\Omega} = \mathbf{A}_T \dot{\mathbf{q}} \quad \dot{\mathbf{q}} = \mathbf{A}_T^{-1} \mathbf{\Omega} = \mathbf{B}_T \mathbf{\Omega} \tag{4}$$

where $\mathbf{\Omega}$ - vector of quasi-velocities, $\mathbf{q}$ – vector of generalized coordinates

$$\mathbf{\Omega} = [\omega_1, \omega_2, ..., \omega_k]^T, \quad \mathbf{q} = [q_1, q_2, ..., q_k]^T \tag{5}$$

The construction of matrix $\mathbf{A}_T$ depends on explored issue. For example, for model of the rigid airplane with movable control surfaces the matrix $\mathbf{A}_T$ has a following construction:

$$\mathbf{A}_T = \begin{bmatrix} \mathbf{A}_G & \mathbf{0} & \mathbf{0} \\ \mathbf{0} & \mathbf{C}_T & \mathbf{0} \\ \mathbf{0} & \mathbf{0} & \mathbf{I} \end{bmatrix} \tag{6}$$

where $\mathbf{I}$ is the unit matrix, $\mathbf{A}_G$ and $\mathbf{C}_T$ are classical matrices of transformations of kinematics and can be found in Ref. [4]. The unit matrix $\mathbf{I}$ has dimension: 14 x 14.

In case when we consider model of aircrafts as systems containing rigid fuselage and *3* elements of longitudinal control system (Fig. 4) the vectors of quasi-velocities, quasi coordinates, and generalized coordinates have the following forms:

$$\mathbf{\Omega} = \left[U, V, W, P, Q, R, \dot{\delta}_H, \dot{\delta}_V, \dot{\delta}_A \right]^T \tag{7}$$

$$\boldsymbol{\pi}_\Omega = \left[\pi_U, \pi_V, \pi_W, \pi_P, \pi_Q, \pi_R, \delta_H, \delta_V, \delta_A \right]^T \tag{8}$$

$$\mathbf{q} = \left[x_s, y_s, z_s, \Psi, \Theta, \Phi, \delta_H, \delta_V, \delta_A \right]^T \tag{9}$$

Matrices $\mathbf{D}_i$ can be determine as follows

$$\mathbf{D}_i = \frac{d\mathbf{a}_i}{d\mathbf{q}} = \begin{bmatrix} \frac{\partial a_{11}}{\partial q_1} & \cdots & \frac{\partial a_{1k}}{\partial q_k} \\ \cdots & \cdots & \cdots \\ \frac{\partial a_{k1}}{\partial q_1} & \cdots & \frac{\partial a_{kk}}{\partial q_k} \end{bmatrix} \tag{10}$$

where the vector $\mathbf{a}_i$ means *i*-th row of the matrix $\mathbf{A}_T$.

In the matrix notation the Boltzmann symbols can be presented in the form of elements of block matrix $\mathbf{\Gamma}$(*k* x (*k* x *k*)):

$$\mathbf{\Gamma} = \begin{bmatrix} \mathbf{\Gamma}^1 \\ \mathbf{\Gamma}^2 \\ \cdots \\ \mathbf{\Gamma}^k \end{bmatrix} = \begin{bmatrix} \mathbf{B}_T{}^T \left(\mathbf{D}_1 - \mathbf{D}_1{}^T \right) \mathbf{B}_T \\ \mathbf{B}_T{}^T \left(\mathbf{D}_2 - \mathbf{D}_2{}^T \right) \mathbf{B}_T \\ ..... \\ \mathbf{B}_T{}^T \left(\mathbf{D}_k - \mathbf{D}_k{}^T \right) \mathbf{B}_T \end{bmatrix} \tag{11}$$

Where $\mathbf{B}_T = \mathbf{A}_T^{-1}$. At last the matrix $\mathbf{\Gamma}$ can be presented in the short matrix form:

$$\mathbf{\Gamma} = \mathbf{B}_T^T \left(\mathbf{D} - \mathbf{D}^T \right) \mathbf{B}_T \tag{12}$$

Finally, Boltzmann-Hamel equations written in the matrix form can be presented as follows:

$$\frac{d}{dt}\left(\frac{\partial T^*}{\partial \mathbf{\Omega}} \right) + \left(\mathbf{\Gamma}^T \mathbf{\Omega} \right) \frac{\partial T^*}{\partial \mathbf{\Omega}} - \mathbf{B}_T^T \frac{\partial T^*}{\partial \mathbf{q}} = \mathbf{Q} - \mathbf{B}^T \frac{U_e}{\partial \mathbf{q}} \tag{13}$$

Eq (14) are very comfortable to use in procedures of automatic formulation of equation of motion.

In the case when we considered dynamics of aircraft with movable control surfaces, and control system elements, vector of quasi-velocities is given by esq. (8). In that case total kinetic energy of the whole system is the sum of the kinetic energy of the rigid fuselage and movable control surfaces, and control elements.

$$T^* = T_s^* + T_H^* + T_V^* + T_A^* \tag{14}$$

According to the general theorem, the kinetic energy of airframe can be calculated as follows::

$$T_s^* = \frac{1}{2} m \mathbf{V}^2 + \frac{1}{2} \mathbf{\Omega}_k^T \mathbf{J}_A \mathbf{\Omega}_k \tag{15}$$

The kinetic energy rudder and elements of longitudinal control system can be calculated from the following formula:

$$T_j^* = \frac{1}{2} m_j \left[\mathbf{V} + \mathbf{\Omega}_k \times \left(\mathbf{R}_j + \mathbf{x}_j \right) + \left(\mathbf{\Omega}_k + \dot{\boldsymbol{\delta}}_j \right) \times \mathbf{R}_j \right]^2 + \frac{1}{2} m_j \dot{\mathbf{x}}_j^2 + \frac{1}{2} \left(\mathbf{\Omega}_k + \dot{\boldsymbol{\delta}}_j \right)^T \mathbf{J}_j \left(\mathbf{\Omega}_k + \dot{\boldsymbol{\delta}}_j \right) \tag{16}$$

where: $\mathbf{R}_j$ – vector connecting centre of gravity of aircraft with axis of rotation (or centre of gravity) of a rudder or *j-th* element of longitudinal control system; $\mathbf{x}_j$ – vector of translation of *j-th* element of control system, $\mathbf{J}_j$ – moment of inertia of rudder or *j*-th element of rotating element of longitudinal control system, $\dot{\boldsymbol{\delta}}_j$ – vector relative angular velocity that rudder or rotating element of longitudinal control system, m_j – mass of *j-th* element.

After making conversions, relation for kinetic energy can be presented in the form:

$$T^* = \frac{1}{2}\mathbf{\Omega}^T \mathbf{E} \mathbf{\Omega} \tag{17}$$

The matrix **E** depends on the mass distribution of airframe and control surfaces, and has the form:

$$\mathbf{E} = \begin{bmatrix} \mathbf{M} & -\mathbf{S}_1 & \mathbf{S}_2^{(E)} \\ \mathbf{S} & \mathbf{J}_A & \mathbf{N}^{(E)} \\ \left(\mathbf{S}_2^{(E)}\right)^T & \left(\mathbf{N}^{(E)}\right)^T & \mathbf{I}_S^{(E)} \end{bmatrix} \tag{18}$$

After making differentiation and conversions we obtain a set of equations describing motion of aircraft with movable control surfaces:

$$\mathbf{E}\dot{\mathbf{\Omega}} + \left(\mathbf{\Gamma}^T \mathbf{\Omega}\right)\mathbf{E}\mathbf{\Omega} - \mathbf{B}^T \mathbf{\Omega}^T \frac{d\mathbf{E}}{d\mathbf{q}}\mathbf{\Omega} = \mathbf{Q} - \mathbf{B}^T \frac{d\mathbf{U}_e}{d\mathbf{q}} \tag{19}$$

Eq (23) with kinematic relations make non-linear set of ordinary differential equations of first kind describing the motion of aircraft with movable control surfaces. These equations are written in the form allowing to create procedures meant for their automatic formulation, (e.g., by means of such well known commercial software as Mathematica® or Mathcad®). The vector **Q** is the sum of aerodynamic loads and another nonpotential forces and moments acting on the aircraft.

2.3. Non-potential loads (vector Q)

2.3.1. Modelling of aerodynamic loads

The adequacy of mathematical modelling of aircraft dynamics is strictly dependent on the adequacy of the aerodynamic model. There is nontrivial problem due to the very complicated nature of the separated and vortex flow in unsteady regime [40]. Precise describing of aerodynamic forces and moments found in equations of motion is fundamental source of difficulties. In each phase of flight dynamics and aerodynamics influence each other, which disturbs the precise mathematical description of those processes. The requirements for method on aerodynamic load calculations stem both from flow environment and from algorithms used in analysis of aircraft flight dynamics. The airframe model consists of the fuselage, horizontal tail, vertical tail, and wings. The fuselage model is based on wind tunnel test data. The horizontal tail and vertical tail were modelled as aerodynamic lifting surfaces with lift and drag coefficients computed from data tables as functions of angle of attack α and slip angle β. To define aerodynamic loads in the nonlinear region of aerodynamic characteristics we attempted the modified strip theory. The modification of the strip, is presented below. We made the following assumptions:

- In given wing cross section resultant aerodynamic force, and aerodynamic moment depend on a local angle of attack.
- The flowfield is disturbed by vector of speed resulting from aircraft rotation (angular rates *P, Q, R*).
- It is included the mutual relation between neighboring strips (by adding the speed induced by flowing down vortex.)
- It is included vortex structures dynamics, and vortex break-down.
- There are included unsteady effect (aerodynamic hysteresis), and stall phenomenon (ONERA deep stall model [39]).

The algorithm of calculations allows defining loads of wings of any shape. In case of modern fighter aircraft, with strongly coupled aerodynamic configuration, it was assumed that lifting fuselage is modeled by the centre wing section. The modified strip theory allows in relatively easy way to consider a phenomenon of asymmetrical vortex break-down (see ref. [45]).Wings are divided into a number of elements (strips). For each strip we calculate a local angle of attack and a airspeed. Then, from airfoil data we find lift, drag and pitching moment coefficients.. Resulting aerodynamic force and moment, is calculated as sum of forces and moments on acting on each strip.. For purpose of numerical analysis, functions $C_L(\alpha)$ and $C_D(\alpha)$ were approximated with trigonometric polynomials:

$$\begin{aligned} C_L(\alpha) &= \sum_{k=0}^{n} [a_k \cos(k\alpha) + b_k \sin(k\alpha)] \\ C_D(\alpha) &= \sum_{k=0}^{n} [c_k \cos(k\alpha) + d_k \sin(k\alpha)] \end{aligned} \tag{20}$$

Where coefficients a_k, b_k, c_k, and d_k were calculated from Runge's scheme. Values of these coefficients are shown in work [20].

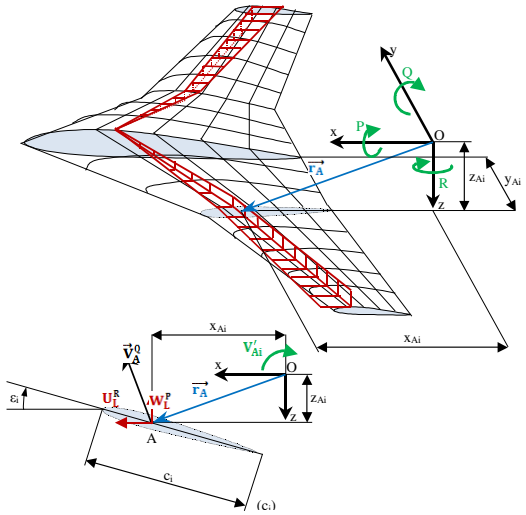

Fig. 5 Distribution of velocities along the wingspan [28]

The angle of attack of α of elementary strip of a wing depends on: the aircraft angle of attack, angle of attack induced by horseshoe vortex and angle of attack induced by airspeed generated by pitch, roll, and yaw angular rates (see fig. 5, and fig. 6)).

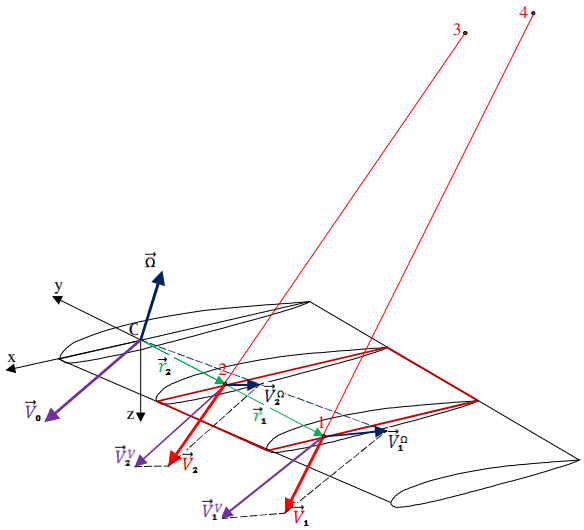

Fig. 6 Distribution of velocities and collocation points along the wingspan, circulation points [28]

The induced angle of attack can be calculated from the relation:

$$\alpha_i = \arctan\left(V_i / V_0\right) \tag{21}$$

The induced speed can be calculated from Biot-Savart's law (fig. 6):

$$\vec{V}_i(y) = \frac{\Delta y}{8\pi b}\sum_{k=1}^{n}\left[C_{zk}c_k\left(\vec{A}_{12_k} + \vec{A}_{23_k} + \vec{A}_{34_k} + \vec{A}_{41_k}\right)\right] \tag{22}$$

Where:

$$\vec{A}_{12} = \frac{\vec{r}_{1k}\times\vec{r}_{2k}}{\left|\vec{r}_{1k}\times\vec{r}_{2k}\right|^2}\left[\vec{r}_{12}\left(\frac{\vec{r}_{1k}}{r_{1k}} - \frac{\vec{r}_{2k}}{r_{2k}}\right)\right] \tag{23}$$

r_1 and r_2 – correspondingly, a distance from left and right bound vortex from point A (in which induced speed is calculated).

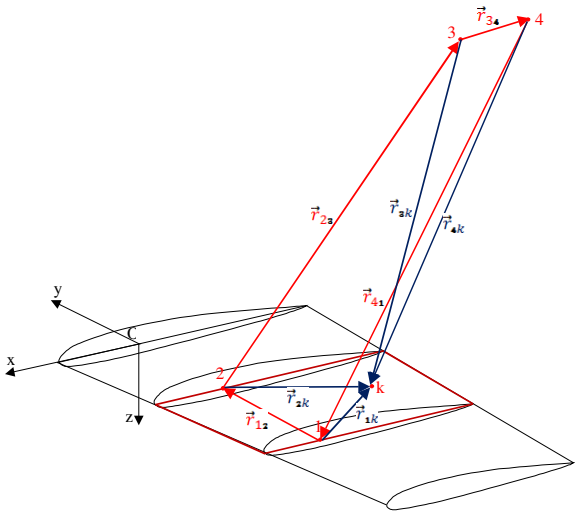

Fig. 7 Allocation of points collocation with strips [28]

Distribution of circulation along wing span can also be calculated with engineer methods (for example, classic Multhopp's method) or evaluated with help of known (for example from examining a plane in aerodynamic tunnel) distribution of pressures along wing span. On the basis of known distribution of circulation we can define distribution of induced angles of attack along wing span (and therefore for each wing's section).

2.3.2. Modeling of freeplay

Due to manufacturing tolerances or loosened mechanical linkages, the connection between a control surface and a servoactuator may have some nonlinearities. For analysis purpose, the nonlinearities can be represented by a nonlinear hinge spring.

The elements of $\{f\}$ in Eq. (24) are zero except for the element representing force exerted by the nonlinear hinge spring of a control surface. This element can be represented by free-play or bilinear nonlinearity. Fig. 8 shows a bilinear spring. The bilinear spring can be expressed as :

$$f(\theta)=\begin{cases} K_\theta\left[\theta-(1-a)\delta\right], & \theta>\delta, \\ aK_\theta\theta, & -\delta<\theta<\delta, \\ K_\theta\left[\theta+(1-a)\delta\right], & \theta<-\delta, \end{cases} \quad (24)$$

where θ and δ are a rudder rotation angle and free-play, respectively. When the stiffness ratio a is zero, Eq. (24) represents a nonlinear spring with free-play.

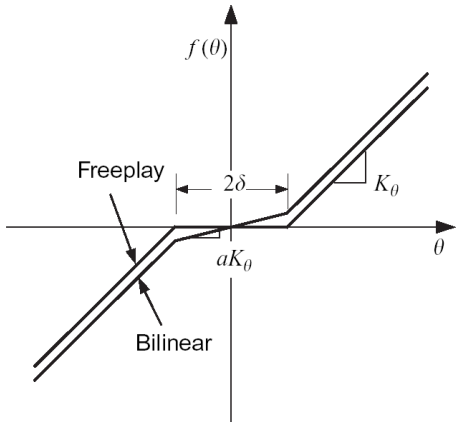

Fig. 8 Free-play and bilinear spring.

For frequency-domain analysis, we need to obtain the equivalent spring from the bilinear spring in Eq. (25). The main idea of the describing function method is to calculate the equivalent spring under the assumption of a harmonic motion. If the motion of the .flap angle θ is harmonic, we can write this as:

$$\theta = A\sin\omega t \quad (25)$$

where A and ω are the amplitude and frequency of harmonic motion, respectively. Considering only the fundamental component, the restoring force can be written as:

$$f(\theta)=K_{eq}\theta \quad (26)$$

Fig. 6 shows the relationship between the LCO amplitude of a rudder responses and the equivalent stiffness.

$$K_{eq}=\begin{cases} aK_\theta, & \le A \le \delta \\ \left[\dfrac{K_\theta}{\pi}\pi-2(1-a)\sin^{-1}\dfrac{\delta}{A}+\right. & \\ \left.-(1-a)\sin\left(2\sin^{-1}\dfrac{\delta}{A}\right)\right], & A\ge\delta \end{cases} \quad (27)$$

As shown in Fig. 9, the equivalent stiffness of a nonlinear spring decreases considerably compared with that of a linear spring and the equivalent stiffness increases as the LCO amplitude increases. The equivalent stiffness of a bilinear spring is larger than that of free-play and the characteristics of a bilinear spring are predicted to be better than those of free-play.

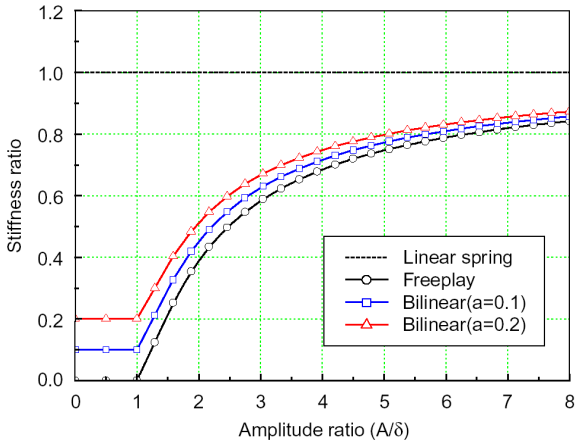

Fig. 9 Equivalent stiffness of nonlinear spring.

Figs. 10-11 show the time history and phase plot for the rudder tip. It is shown that two different types of LCO occur. One is LCO 1 with low frequency (19.7 Hz) and the other is LCO 2 with high frequency (61.2 Hz). Due to the difference of the .utter mode, the tip amplitude of LCO 1 is larger than that of LCO 2 whereas the flap amplitudes of LCO 1 and LCO 2 are almost the same. These LCO types are dependent on an initial flap amplitude.

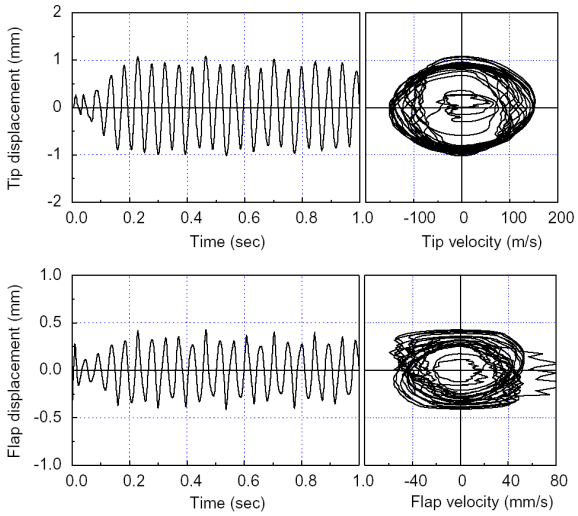

Fig. 10 Example of simulation of rudder motion (θ/δ=1.5)

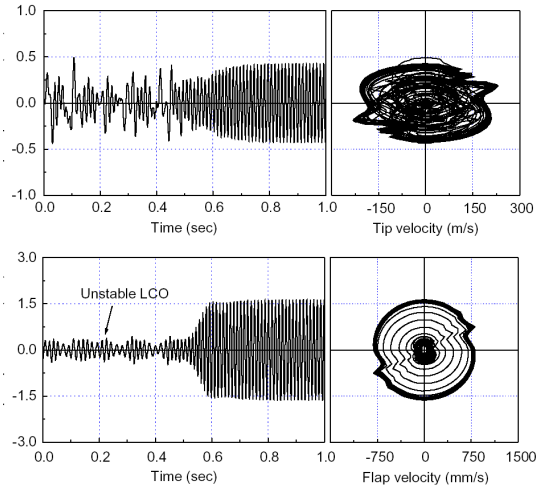

Fig. 11 Example of simulation of rudder motion (θ/δ=1.0)

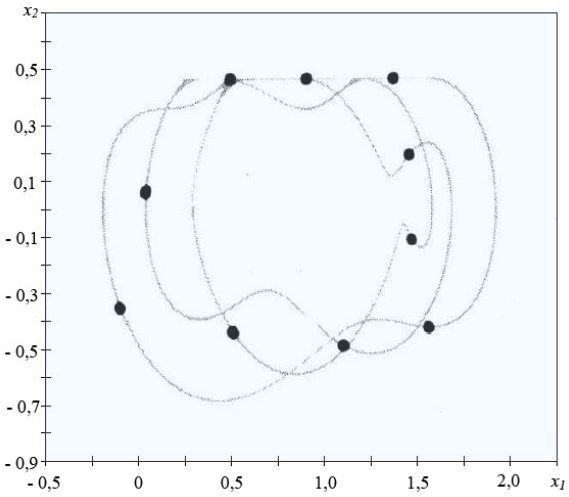

Fig. 12 Phase portraits and Poincaré maps of multi – periodic motion. Naminal stiffness of system: k_1+k_2= 140 MN/m

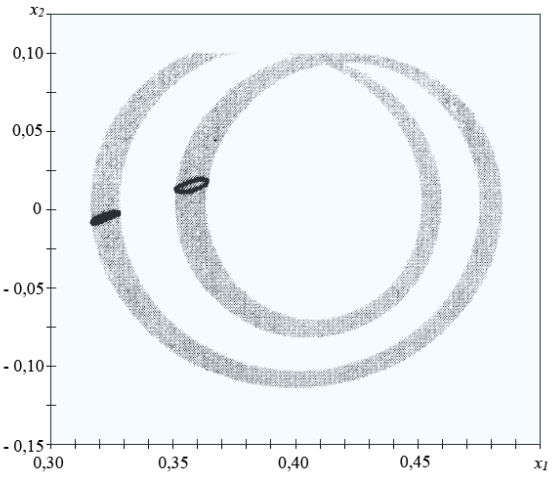

Fig. 13 Phase portraits and Poincaré maps of quasi – periodic motion. Stiffness of system k_1+k_2= 14 MN/m

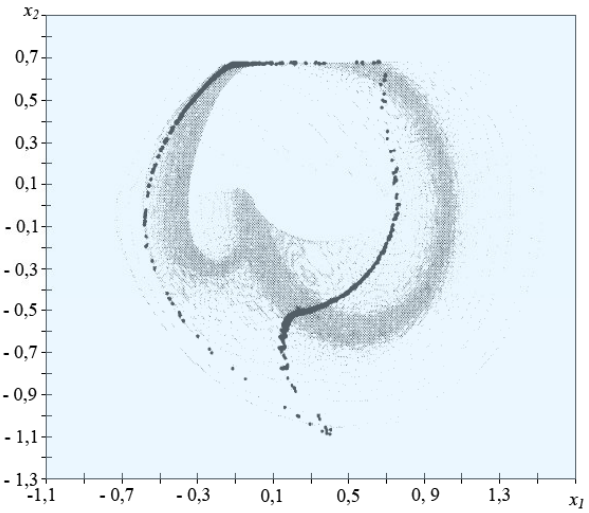

Fig. 14 Phase portraits and Poincaré maps of chaotic motion. Stiffness of system k_1+k_2= 14 kN/m

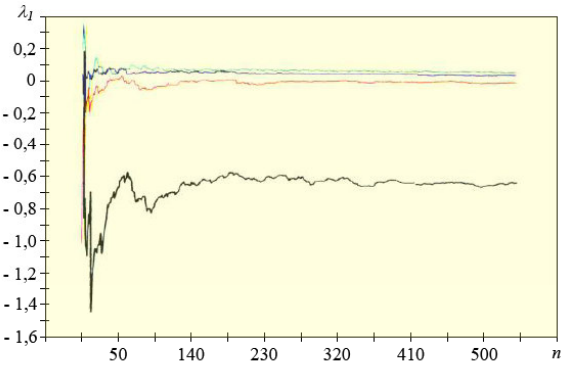

Fig. 15 Lyapunov multipliers for situation shown in Fig 14. Chaotic motion

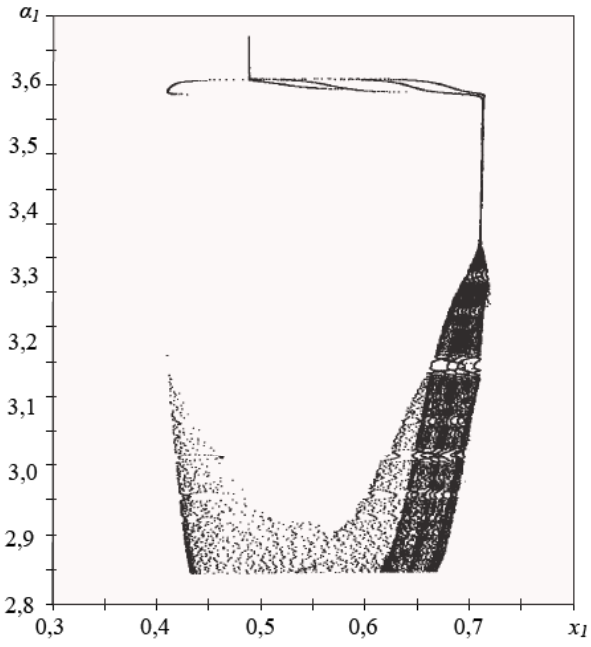

Fig. 16 Bifurcation diagram. Stiffness of system 14kN/m

Figures 12, 13, 15, 15, and 16 show response of the representative mass of aircraft longitudinal control system (Fig. 3). Parameter x_1 denote undimensional longitudinal displacement of mass m defined as: $x_1 = \frac{k_2}{\mu_0 mg} x$, where: x means displacement of mass m, k_2 is stiffness of control system (as shown in Fig. 3), μ_0 is coefficient of static friction, g is gravitational acceleration. Parameter x_2 is time derivative of x_1: $x_2 = \frac{dx_1}{d\tau} = \frac{k_2}{\mu_0 mg} \frac{dx}{d(\omega t)} = \frac{k_2}{\mu_0 mg\omega} \frac{dx}{dt}$, where $\omega = \sqrt{\frac{(k_1 + k_2)}{m}}$. We define the driving space defined by the maximum static friction force of aircraft longitudinal control system, and we have found the domains, in which chaotic behaviors of control system is possible. The time period for the simulation was 2400 seconds. During computations, one half of the time period corresponds to the time interval, where transitional processes are damped. We assume 3 different stiffness of control system: nominal (k=140 MN/m), 100 times lower (k=1.4 MN/m), and 10000 times lower (k=14 kN/m). In the case of nominal stiffness (Fig. 12) multi periodic oscillation of control system occurred. When the stiffness is 100 times lowering, quasi periodic motion occurred (Fig. 13). Fig 14 shows chaotic oscillations in longitudinal control system, that occurred in the case of very low stiffness of control system (k=14 kN/m). The chaotic nature of oscillations in the 3rd case of stiffness was confirmed by calculation of Lyapunow multipliers (Fig. 15). The bifurcation diagram for chaotic oscillations is shown in Fig. 16.

2.3.3 Modeling of unilateral contact conditions with application to aircraft control system involving backlash and friction

Joints impose constraints on the relative motion of the various bodies of the system. Most joints used for practical applications can be modeled in terms of the so called lower pairs [22]: the revolute, prismatic, screw, cylindrical, planar and spherical joints. If two bodies are rigidly connected to one another, their six relative motions, three displacements and three rotations, must vanish at the connection point. If one of the lower pair joints connects the two bodies, one or more relative motions will be allowed. For instance, the revolute joint allows the relative rotation of two bodies about a specific body attached axis while the other five relative motions remain constrained. The constraint equations associated with this joint are presented above.

Consider two bodies denoted with superscripts $(.)^k$ and $(.)^l$, respectively, linked together by a revolute joint, as depicted in Fig. 17. In the reference configuration, the revolute joint is defined by coincident triads $\mathcal{S}_0^k = \mathcal{S}_0^l$, defined by three unit vectors $\mathbf{e}_{10}^k = \mathbf{e}_{10}^l$, $\mathbf{e}_{20}^k = \mathbf{e}_{20}^l$, and $\mathbf{e}_{30}^k = \mathbf{e}_{30}^l$. In the deformed configuration, the orientations of the two bodies are defined by two triads, $\mathcal{S}^k$ (with unit vectors $\mathbf{e}_1^k, \mathbf{e}_2^k$, and $\mathbf{e}_3^k$), and $\mathcal{S}^l$ (with unit vectors $\mathbf{e}_1^l, \mathbf{e}_2^l$, and $\mathbf{e}_3^l$). The kinematic constraints associated with a revolute joint imply the vanishing of the relative displacement of the two bodies while the triads $\mathcal{S}^k$ and $\mathcal{S}^l$ are allowed to rotate with respect to each other in such a way that $\mathbf{e}_3^k = \mathbf{e}_3^l$. This condition implies the orthogonality of $\mathbf{e}_3^k$ to both $\mathbf{e}_1^l$ and $\mathbf{e}_2^l$. These two kinematic constraints can be written as:

$$C_1 = \mathbf{e}_3^{kT} \mathbf{e}_1^l = 0 \tag{28}$$

and

$$C_2 = \mathbf{e}_3^{kT} \mathbf{e}_2^l = 0 \tag{29}$$

In the deformed configuration, the origin of the triads is still coincident. This constraint can be enforced within the framework of finite element formulations by Boolean identification of the corresponding degrees of freedom.

The relative rotation 4 between the two bodies is defined by adding a third constraint

$$C_3 = \left(\mathbf{e}_1^{kT} \mathbf{e}_1^l\right) \sin\phi + \left(\mathbf{e}_1^{kT} \mathbf{e}_2^l\right) \cos\phi = 0 \tag{30}$$

The three constraints defined by eqs. (28) to (30) are nonlinear, holonomic constraints that are enforced by the addition of constraint potentials $\lambda_i C_i$, where λ_i, are the Lagrange multipliers. Details of the formulation of the

constraint forces and their discretization can be found in Refs. [20 21].

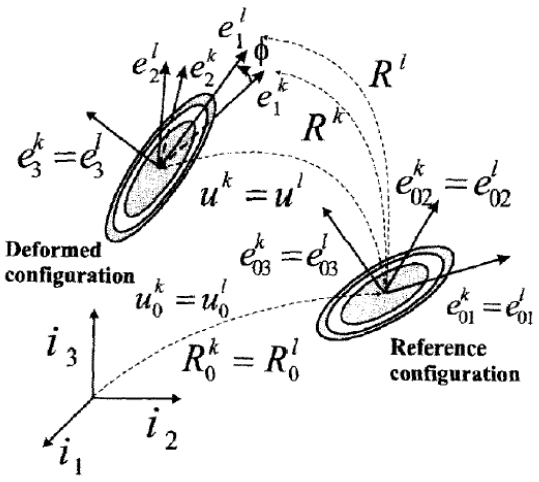

Fig. 17 Revolute joint in the reference and deformed configurations. [cf. [24])

A revolute joint with backlash is depicted in Fig. 11(a. The backlash condition will ensure that the relative rotation ϕ, defined by eq. (30), is less than the angle ϕ_1, and greater than the angle ϕ_2 at all times during the simulation: i.e. $\phi_1 \geq \phi \geq \phi_2$, ϕ_1 and ϕ_2 define the angular locations of the stops. When the upper limit is reached, $\phi = \phi_1$, a unilateral contact condition is activated. The physical contact takes place at a distance R_1, from the rotation axis of the revolute joint. The relative distance q_1 between the contacting components of the joint writes

$$q_1 = R_1(\phi_1 - \phi) \qquad (31)$$

When the lower limit is reached, $\phi = \phi_2$, a unilateral contact condition is similarly activated. The relative distance q_2 then becomes

$$q_2 = R_2(\phi 2 - \phi) \qquad (32)$$

where R_2 is the distance from the axis of rotation of the revolute joint

If the stops are assumed to be perfectly rigid, the unilateral contact condition is expressed by the inequality $q > 0$, where the relative distance q is given by eq. (34) or (35). This inequality constraint can be transformed into an equality constraint $q - r^2 = 0$ through the addition of a slack variable r. Hence, the unilateral contact condition is enforced as a nonlinear holonomic constraint

$$C = q - r^2 = 0 \qquad (33)$$

This constraint is enforced via the Lagrange multiplier technique. The corresponding forces of constraint are

$$\delta C\lambda = \begin{bmatrix} \delta q \\ \delta r \end{bmatrix}^T \begin{bmatrix} \lambda \\ -\lambda 2r \end{bmatrix} = \begin{bmatrix} \delta q \\ \delta r \end{bmatrix} \mathbf{F}^C \qquad (34)$$

where λ is the Lagrange multiplier. To obtain unconditionally stable time integration schemes [23, 24] for systems with contacts, these forces of constraint must be discretized so that the work they perform vanishes exactly. The following discretization is adopted here

$$\mathbf{F}_m^c = \begin{bmatrix} s\lambda_m \\ -s\lambda_m 2r_m \end{bmatrix} \qquad (35)$$

where s is a scaling factor for the Lagrange multiplier, λ_m the unknown midpoint value of this multiplier, and $r_m = (r_f + r_i)/2$. The subscripts $(.)_f$ and $(.)_i$ are used to indicate the value of a quantity at the initial time t_i, and final time t_f of a time step of size Δt. respectively. The work done by these discretized forces of constraint is easily computed as $W^c = C_t - C_i)\lambda_m$. Enforcement of the condition $C_f = C_i = 0$ then guarantees the vanishing of the work done by the constraint forces. The Lagrange multiplier λ_m is readily identified as the contact force.

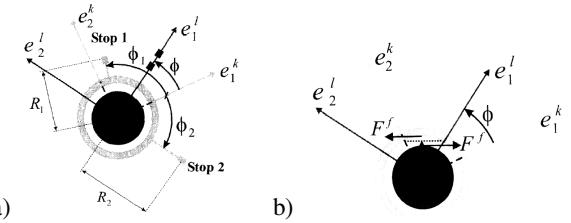

Fig. 19 a) A revolute joint with backlash. The magnitude of the relative rotation ¢ is limited by the stops;
b) A revolute joint with friction. (cf. [23, 24]

For practical implementations, the introduction of the slack variable is not necessary. If at the end of the time step $q_f \geq 0$, the unconstrained solution is accepted and the simulation proceeds with the next time step. On the other hand, if $q_f < 0$ at the end of the time step, the step is repeated with the additional constraint $q_f = q_i$ and the Lagrange multiplier associated with this constraint directly represents the contact force.

In general, the stops will present local deformations in a small region near the contact point. In this case the stops are allowed to approach each other closer than what would be

allowed for rigid stops. This quantity is defined as the approach and is denoted *a*; following the convention used in the literature [9], $a > 0$ when penetration occurs. For the same situation, $q < 0$, see eqs. (33) and (34). When no penetration occurs, $a = 0$, by definition, and $q > 0$. Combining the two situations leads to the contact condition $q + a \geq 0$, which implies $q = -a$ when penetration occurs. Here again, this inequality condition is transformed into an equality condition $C = q + a - r^2 = 0$ by the addition of a slack variable *r*. When the revolute joint hits a deformable stop, the contact forces must be computed according to a suitable phenomenological law relating the magnitude of the approach to the force of contact [23,24]. In a generic sense, the forces of contact can be separated into elastic and dissipative components. As suggested in ref. [24], a suitable expression for these forces is

$$\begin{aligned}\mathbf{F}^{contact} &= \mathbf{F}^{elas} + \mathbf{F}^{diss} = \frac{dV}{da} + \frac{dV}{da} f^d(\dot{a}) \\ &= \frac{dV}{da}\left[1 + f^d(\dot{a})\right]\end{aligned} \tag{36}$$

where *V* is the potential of the elastic forces of contact, and $f_d(\dot{a})$ accounts for energy dissipation during contact. In principle, any potential associated with the elastic forces can be used; for example, a quadratic potential corresponds to a linear force-approach relationship, or the potential corresponding to the Hertz problem. The particular form of the dissipative force given in eq. (37) allows to define a damping term that can be derived from the sole knowledge of a scalar restitution coefficient, which is usually determined experimentally or it is readily available in the literature for a wide range of materials and shapes [23].

When sliding takes place, Coulomb's law states that the friction force $\mathbf{F}^f$ is proportional to the magnitude of the normal contact force $\mathbf{F}^n$

When sliding takes place, Coulomb's law states that the friction force $\mathbf{F}^f$ is proportional to the magnitude of the normal contact force $\mathbf{F}^n$

$$\mathbf{F}^f = -\mu_k(V_r)\mathbf{F}^n \frac{V_r}{|V_r|} \tag{37}$$

where $\mu_k(V_r)$ is the coefficient of dynamic friction and $|V_r|$ the magnitude of the relative velocity tangent to the plane, V_r. If the relative velocity vanishes, sticking may take place if the following inequality is met

$$|\mathbf{F}^f| \leq \mu_s F^n \tag{38}$$

where μ_s is the coefficient of static friction. A revolute joint with friction is shown in fig. 4. In this case, the relative velocity, V_r is given by $V_r = \rho\dot{\phi}$, where ρ is the radius of the inner and outer races and $\dot{\phi}$ the relative rotation. When the races stick together, the relative velocity $\dot{\phi}$ vanishes, resulting in the following linear non-holonomic constraint,

$$\dot{\phi} = 0 \tag{39}$$

Application of Coulomb's law involves discrete transitions from sticking to sliding and vice-versa, as dictated by the magnitude of the friction force and the vanishing of the relative velocity, eqs (36) and (37)) respectively. These discrete transitions can cause numerical difficulties, and numerous authors have advocated the use of a continuous friction law [23, 24], typically written as

$$\mathbf{F}^f = -\mu_k(V_r)\mathbf{F}^n \frac{V_r}{|V_r|}\left(1 - e^{|V_r|/v_0}\right) \tag{40}$$

where v_0, is a characteristic velocity usually chosen to be small compared to the maximum relative velocity encountered during the simulation. $\left(1 - e^{|V_r|/v_0}\right)$ is a "regularizing factor" that smoothes out the friction force discontinuity. The continuous friction law describes both sliding and sticking behavior, i.e. it replaces both eqs. (37) and (38). Sticking is replaced by "creeping" of the inner race with respect to outer race at small relative velocity. Various forms of the regularizing factor have appeared in the literature.

However, the use of a continuous friction law presents a number of shortcomings [24]:

1) it alters the physical behavior of the system and can lead to the loss of important information such as large variations in frictional forces;

2) it negatively impacts the computational process;
3) it does not appear to be able to deal with systems with different values of the static and kinetic coefficients of friction. Consequently, friction effects will be modeled in this work through a combination of Coulomb's friction law and the enforcement of the sticking constraint.

In practice, it is not convenient to determine the exact instant when the relative velocity vanishes: i.e. when $V_r = 0$. Rather, the sticking constraint, eq. (40), is enforced when $V_r < v_0$, where v_0 is an appropriately selected characteristic relative velocity.

3 Bifurcation analysis of aircraft dynamics

A wide collection of useful numerical algorithms for the exploration of ordinary differential equations has been made available through the public domain software XPPAUT[2] [5]. With its graphical interface to the popular continuation and bifurcation software AUTO, XPPAUT combines the advantages of two worlds: A set of ordinary differential equation can be integrated with the phase plane explorer XPP until a steady-state has been reached; once balanced, the system equations can then be passed to AUTO97[3] for continuation and bifurcation analysis

In our work we concerned with static bifurcations, i.e. bifurcations associated with changes in the equilibrium point structure. There is a fundamental difference between bifurcation analysis of dynamical systems and control systems. As seen above, the behavioral aspects at the bifurcation points of control systems involve issues of system controllability, observability, et cetera, which are nonexistent for dynamical system bifurcation analysis. In addition to the limiting points that arise from static bifurcation points, we are also interested in limitations due to loss of stability and functional actuator limits. The bifurcation analysis is the same for the open and closed loop cases. However, the analysis of stability, and the characteristics of the system at the bifurcation points are different for the two cases. The equilibrium equations are simpler for the open loop system. Once we have obtained the bifurcation curves for the open loop system, the closed loop bifurcation curves can be obtained using the control law.

A failure via a stuck actuator alters the structure of the control system. The stuck control surfaces not only ceases to be a viable input, but also acts as a persistent disturbance on the system. The reconfigured controller is designed as a regulator with disturbance rejection properties. The nonlinear regulator problem is to determine a feedback control law that guarantees asymptotic stability of the closed loop system and ensures that the regulated variables specified by equation have the prescribed steady state value. The control law requires information about both the states and the disturbance, i.e., the stuck actuator position. This information can be obtained through measurements of an observer. The observer dynamics and design are not relevant to the bifurcation analysis. We reduce the number of control inputs of the nominal system to one by setting $\delta_{el} = \delta_{er}$, in order to satisfy the conditions for designing regulators With conditions for straight and level flight. Also by substituting $Q = 0$ results in the right side of the three state equations $\dot{U} = 0$, $\dot{W} = 0$, $\dot{Q} = 0$ being exactly zero, satisfying equilibrium condition for these equations. Dropping these three equations simplifies the analysis by allowing larger increments in the bifurcation parameter values.

For the nominal system, we carry out the bifurcation analysis with the velocity V as the bifurcation parameter. For each of the actuator failures, namely, a stuck elevator, we carry out two kinds of bifurcation analysis. First, for each kind of failure, we consider the control surface to be stuck at it's trim value, and treat the velocity as the parameter. Second, we hold the velocity fixed at the nominal value of 110 *m/s* and vary the stuck position of the failed actuator. The bifurcation curves with velocity as

[2] XPPAUT is a WINDOWS® version of well known AUTO software available at internet address: http://www.math.pitt.edu/~bard/xpp/xppwin.html
[3] AUTO97 is very powerful public domain software available at the address: http://indy.cs.concordia.ca/auto/

the parameter for the nominal and the reconfigured systems for each kind of failure are shown in Figure 20. The curves shown are with respect to the elevator surface deflection. The same information can be obtained with the bifurcation curves plotted with respect to. the other states. These curves are qualitatively similar although they can differ somewhat in shape.

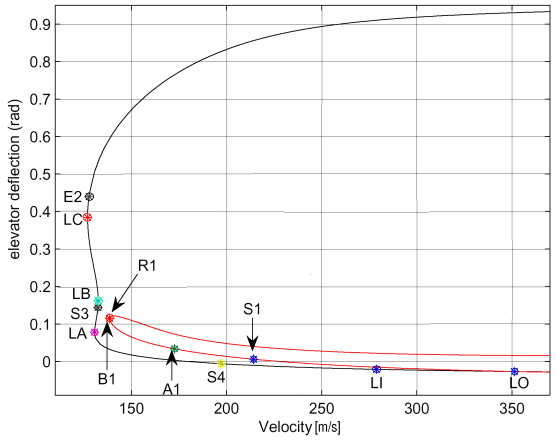

Fig. 20 Bifurcation curves of the nominal and reconfigured systems with single actuator failures and velocity as the parameter

The black plot corresponds to the nominal system. Three bifurcation points, LA (130.7 m/s), LB (132.6 m/s) and LC (127 m/s) can be identified on the equilibrium surface. At these three points both the open and closed loop systems are unstable. The linearized system at these points has transmission zeros at the origin, is uncontrollable and has dependent inputs. The open loop system is unstable at all values of the velocity parameter. The closed loop is designed to be stable at LO (351 m/s). However, at velocities lower than 279 m/s corresponding to the equilibrium point LI the closed loop system becomes unstable. We can also identify actuator limits on the equilibrium surface. The point E2 (127.7 m/s) corresponds to the elevator upper limit. Analysis for straight and level flight with a stuck rudder at trim respectively result in the same equilibrium surface. The reconfigured systems for the elevator failure have different stability boundaries, closed loop system is unstable for speeds lower than S3 (132.4 m/s) and S4 (197 m/s) with the appropriate regulators. The linearization at the bifurcation points LA, LB, and LC, for the reconfigured control systems for elevator failures have dependent inputs, are uncontrollable, unobservable and have two transmission zeros at the origin. The reconfigured system with a stuck elevator results in a qualitatively different equilibrium surface shown in red in the Fig. 20. It has only one bifurcation point identified as B1 (138.5 m/s) at which the linearized system is unstable and is uncontrollable, unobservable, has dependent inputs and one transmission zero at the origin. The reconfigured system becomes unstable at velocities lower than 214 m/s marked by S1. The upper elevator limits are marked on the surface at A1 (172.7 m/s) and R1 (138.5 m/s) respectively.

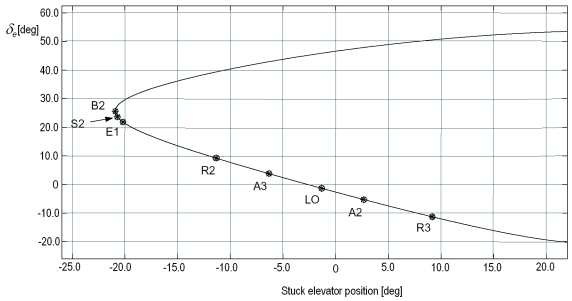

Fig. 21 Bifurcation curve of the system with a stuck elevator and the stuck position as the parameter.

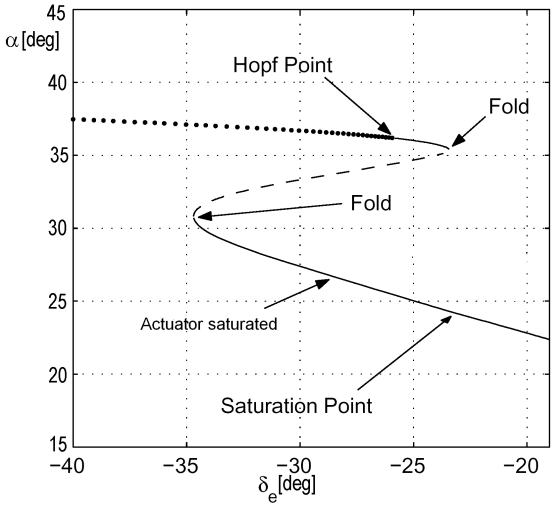

Fig. 22 Bifurcation curve of the system with actuator saturation – high α branch

The bifurcation curves for the reconfigured elevator failure, aileron failure and rudder failure are shown in figures 21, and 22. The reconfigured system for the stuck left elevator first encounters the aileron actuator limits. A2

(3 deg.) and A3 (-7.2 deg) correspond to the allowable lower and upper elevator deflection. Next it encounters the elevator limits: R2 (-13 deg.) is the lower limit and R3 (10.5 deg.) is the upper limit. The elevator reaches its saturation point at E1 (-23 deg.).

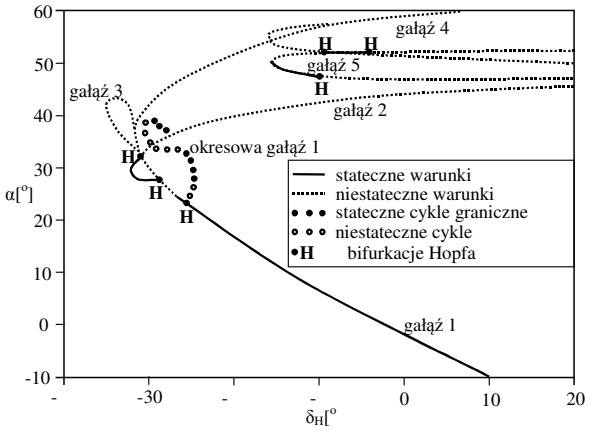

Fig. 23 Global bifurcation diagram [15]

The global bifurcation diagram of angles of attack a for the stabilator sweep is shown in Fig. 23. Branch 1, the branch continued from the initial starting point, has zero lateral states along its entire length. Branches 2 and 5, which all result from pitchfork bifurcations, have non-zero lateral states and each represents two branches which are symmetric with respect to the *Oxz* plane. The periodic branch emanating from the Hopf bifurcation on branch 1 is also shown. If we assume that the aircraft is in equilibrium at the starting point of $\alpha = 10$ deg., then, as the stabilator deflection is increased (more negative) statically, the equilibrium point progresses along branch 1. This would be true assuming no disturbance, such as a wind gust, is large enough to result in a jump to another stable state along another equilibrium branch or periodic branch. As the stabilator deflection reaches the value at which the Hopf bifurcation occurs, branch 1 becomes unstable. A Hopf bifurcation occurs when a complex-conjugate pair of poles crosses the imaginary axis into the right half-plane. The unstable equilibrium is an unrealizable state since the smallest disturbance will cause the state trajectory to diverge from equilibrium. Therefore, as the stabilator deflection increases past the critical value at the Hopf bifurcation point, a jump must occur to another attractor, in this case, to the limit cycle represented by periodic branch 1 at this elevator deflection. The phenomenon which causes this jump occurs during the transition from the stable equilibrium portion of branch 1 to the stable limit-cycle portion of periodic branch 1. This jump actually represents the onset of wing rock, and the trigger point is the Hopf bifurcation point located on branch 1. This point occurs at $\alpha = 25$ deg. Wing rock begins here, and we will demonstrate later on that this coincides with the complex-conjugate pair of Dutch-roll eigenvalues migrating into the right half-plane. This point will be critical to the remainder of the analysis.

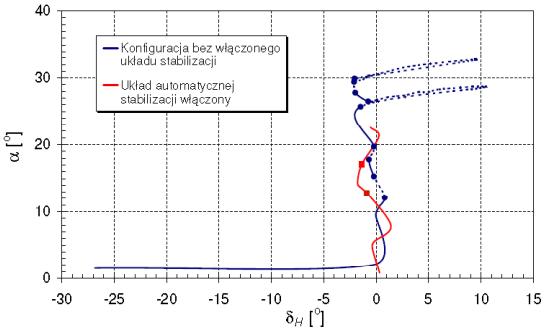

Fig. 24 Steady states of the basic aircraft model, SCAS - off model blue line, SCAS – on model red line, $\delta_A = \delta_V = 0$: —— stable; - - - - unstable; ● Hopf bifurcation; ■ pitchfork bifurcation

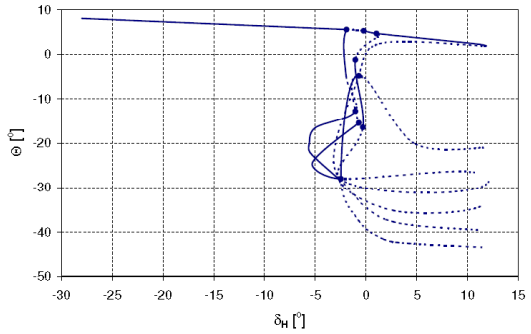

Fig. 25 Steady states of the basic aircraft model, SCAS - off model blue line; $\delta_A = \delta_V = 0$: —— stable; - - - - unstable; ● Hopf bifurcation

The results of calculations shown in Figs. 24, and 25 are for the basic airframe, unaugmented (blue line) and augmented (red line) model. For unaugmented model we can see a mild longitudinal instability at subsonic speed. Figure 25 shows the continuation diagrams of angle of attack α vs the stabilator angle δ_H, for $\delta_A = \delta_V = 0$. Figure 26 shows the continuation diagrams

of pitch angle Θ, vs the stabilator angle δ_H, for $\delta_A = \delta_V = 0$. As expected, several unstable segments lie on the branch of symmetrical equilibria due to the negative static margin of the aircraft. It is apparent that small deflections of the stabilator are required for trimming the aircraft, inasmuch as the reduced level of trim drag associated with this characteristic is one of the reasons that led to the choice of flying an unstable aircraft [1]. A second stable branch is visible in the $-\delta_H$ plot for $\alpha \leq 11{,}8$ deg and represents the steady states that are realized when, aircraft has static stability and the nose-down stabilator effectiveness is lost. In advertent excursions to this range of α are inhibited by the α /a_n limiting system of the augmented aircraft. Figure 25 shows (red line) the bifurcation diagrams of the same states as just described vs the stabilator deflection for the complete aircraft model with SCAS, in α - command mode. The sideslip angle was very small in all of the continuations due to the actions of both the ARI and the yaw damper and is not reported in the Figures. As a general comment we note that this mode of operation produces a rather conventional steady-state response of the aircraft stability until the longitudinal command is saturated at $\alpha = 23$ deg. Also, Fig. 25 shows, that for the aircraft model featuring high augmentation, the steady states present a completely different structure when the SCAS is active.

Results of simulations

The figures 26, 27. 28, 29, and 30 show the response of the aircraft under ruder disturbance in the case of present of free-play and friction in control system. This figures show influence of free-play and friction of aircraft dynamics. We can observed irregular response of elevator, as well as selected flight parameters.

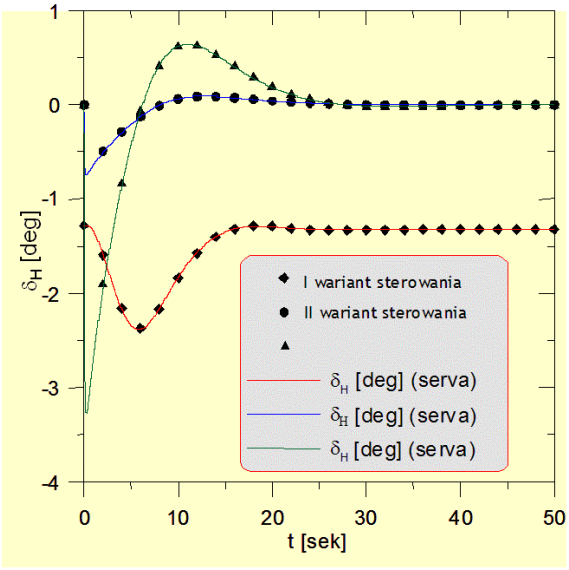

Fig. 26 Results of simulations. Deflection of rudder - no friction and free-play in control system

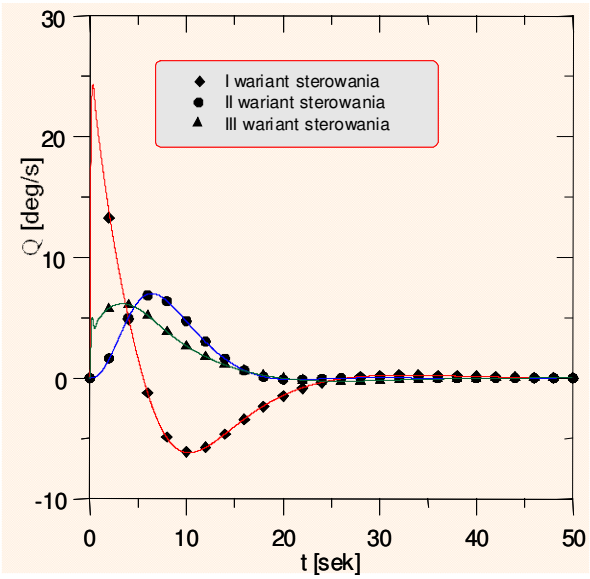

Fig. 27 Results of simulations. Course of pitch angle - no friction and free-play in control system

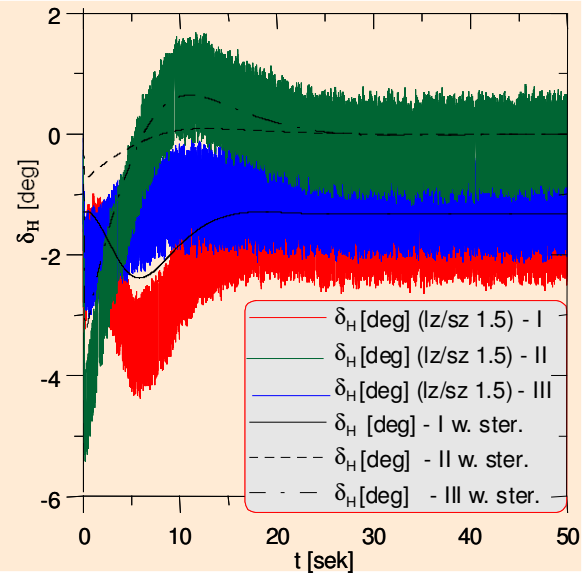

Fig. 28 Influence of free-play on rudder dynamics Angle of tree-play $l_z/t_{c1}=\delta$=1.5.

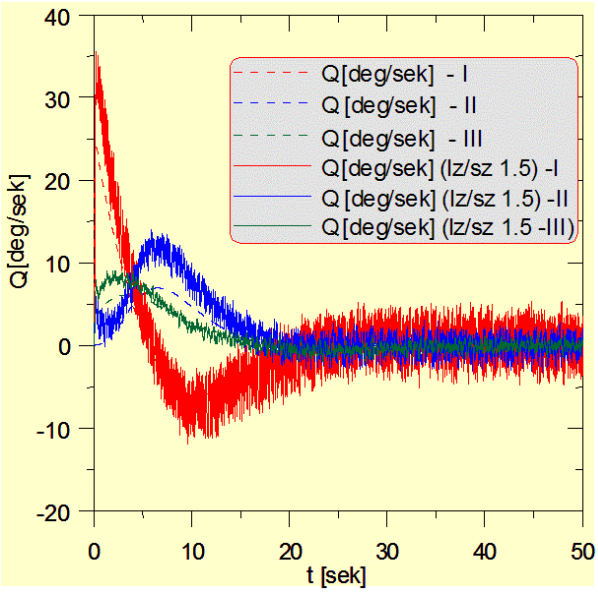

Fig. 29 Influence of free-play on longitudinal aircraft dynamics. Angle of tree-play $l_z/t_{c1}=\delta$=1.5.

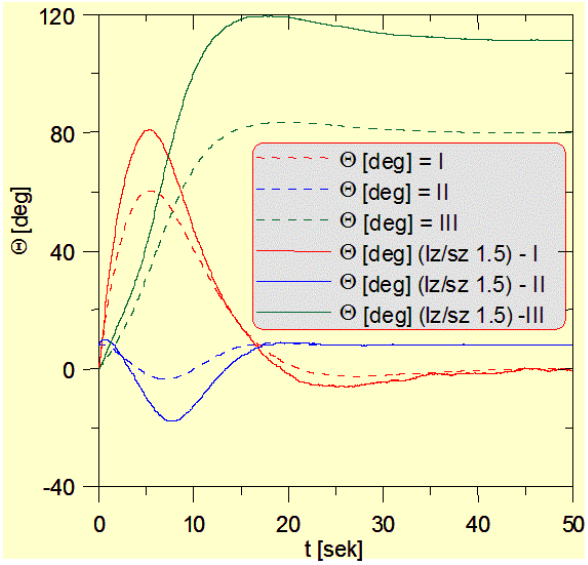

Fig. 30 Influence of free-play on longitudinal aircraft dynamics. Angle of tree-play $l_z/t_{c1}=\delta$=1.5.

6. Conclusions

In many applications the hydraulic servo-actuators are superior to electrical ones, there are applications where the relative simplicity of electrical drive is preferred. Free play effect can radically change the response of aircraft. In this work we calculated static bifurcation points for the fighter aircraft in straight and level flight, for the nominal and various reconfigured systems for single stuck actuators. The analysis was performed for a full envelope nonlinear model of aircraft, allowing for large variations in the parameters. In applying the continuation method to aircraft dynamics several numerical issues were addressed. This work will aid the automation of bifurcation analysis for control systems which is ongoing work. This will help us to identify the complete maneuverability envelope associated with actuator failures and see how the post fault operating conditions differ from the operating conditions

References

[1] Avanzini G., De Matteis G., Bifurcation analysis of a highly augmented aircraft model, *Journal of Guidance, Control & Dynamics,* Vol.20,No.1, 1998.

[2] Bajpai, G., Chang, B. C., and Kwatny, H. G., Design of fault-tolerant systems for actuator failures in nonlinear systems, *American Control Conference*, Vol. 5, IEEE, May 2002, pp. 3618–3623.

[3] Bauchau O. A. and . Rodriguez J.; Simulation of wheels in nonlinear, flexible multi-body systems. *Multibody System Dynamics,* 2001

[4] Bauchau O. A., Bottasso C., and Rodriguez J., Modeling of unilateral contact conditions with application to aerospace aystems involving backlash, freeplay and friction, *Mechanics Research Communication*, Vo. 28, No 4, 2001, pp 571-599.

[5] Crawford I. E., Introduction to Bifurcation Theory, *Reviews of Modern Physics*, Vol. 63, No. 4, 1991.

[6] Doedel E., Kernevez J. P., *AUTO – software for continuation and bifurcation problems in ordinary differential equations*, Caltech, Pasadena 1986.

[7] Ermentrout B., *Simulating, Analyzing, and Animating Dynamical Systems. A Guide to XPPAUT for Researchers and Students*, SIAM, Philadelphia, 2002

[8] Fielding, C., Varga, A., Bennani, S. and Selier, M. (Eds.) Advanced Techniques for Clearance of Flight Control Laws, Lecture Notes in Control and Information Sciences no. 283, Springer, 2002.

[9] Goman M.G., Khramtsovsky A.V., Application of continuation and bifurcation methods to the design of control systems. *Phil. Trans. R. Soc.*, No. A 356, London, 1998, pp 2277-2295.

[10] Guckenheimer J., Holmes J., *Nonlinear Oscillations, Dynamical Systems, and Bifurcations of Vector Fields*, Springer, N. Y., 1983.

[11] Guicheteau P., Bifurcation Theory in Flight Dynamics an Application to a real Combat Aircraft, ICAS-90-5.10.4, *Proceedings of 17th ICAS Congress*, Stockholm, Sweden, 1990.

[12] Harpur, N..F. : Some design considerations of Hydraulic Servos of the Jack type, Proc. of the conf. on Hydraulic Servo mechanisms .Proc. Inst. Mech. Eng.,(UK) p 41 (1953).

[13] Ioos G., Joseph D., *Elementary Stability and Bifurcation Theory*, Springer-Verlag, New York, 1980.

[14] Jahnke C. C., Culick F. E. C., Application of Bifurcation Theory to the High-Angle-of-Attack Dynamics of the F-14, *Journal of Aircraft*, Vol. 31, No. 1, pp.26-34, 1994

[15] Liebst B, The dynamics, prediction, and control of wing rock in high-performance aircraft, *Phil. Trans. R. Soc. Lond.* A **356**, 1998, pp. 2257, 2276.

[16] Lowenberg M. H.. Bifurcation Analysis of Multiple-Attractor Flight Dynamics. *Phil. Trans. R. Soc.,* No. A 356, London, 1998, pp. 1745:2297-2319.

[17] Marsden J. E., McCracken M., The Hopf Bifurcation and its Applications, *Applied Mathematical Science,* v. 19, Springer Verlag, New York, 1976.

[18] Marusak A. J., Pietrucha J. A., Sibilski K. S., Prediction of Aircraft Critical Flight Regimes Using Continuation and Bifurcation Methods, AIAA Paper, AIAA-2000-0976, *38th Aerospace Sciences Meeting and Exhibit,* Reno, NV, January, 2000

[19] Narkiewicz J., Rotorcraft Aeromechanical and Aeroelastic Stability, *Scientific Works of Warsaw University of Technology, Issue Mechanics*, no. 158, 1994.

[20] Rohacs J.: Analysis of methods for modeling real flight situations, 17tb Congress of ICAS. Stockholm Sweden. 1990. *ICAS Proceedings 1990.* pp. 2046.2056

[21] Sibilski K., An Agile Aircraft Non-Linear Dynamics by Continuation Methods and Bifurcation Theory, *ICAS-2000-712, Proceedings of 22nd ICAS Congress*, Harrogate, UK, 2000.

[22] Sibilski K., *Modelling and simulation of flying vehicles dynamics,* MH, Warsaw, 2004.

[23] Sibilski K., Wroblewski W., The influence of free play and friction in longitudinal control system on the strike aircraft longitudinal aircraft dynamics, *Proceedings of thw 25th ICAS Congress,* Hamburg, Germany. 2006

[24] Thomas, S., et all., Nonlinear dynamics, stability & bifurcation in aircraft: simulation and analysis tools, AIAA 2005-6428CP, *AIAA Guidance, Navigation, and Control Conference and Exhibit,* August, 2005

[25] Tran C. T., Petot D., Semi-Empirical Model for the Dynamic Stall of Airfoils in View of the Application to the Calculation of Responses of a Helicopter Rotor Blade in Forward Flight, *Vertica*, 5, 1981.

[26] Troger H., Steindl A., *Nonlinear Stability and Bifurcation Theory*, Springer Verlag, New York, 1991.

[27] Wiggins S., *Introduction to Applied Nonlinear Dynamical Systems and Chaos*, Springer-Verlag, New York, 1990.

[28] Wróblewski W., *Influence of free play and friction in longitudinal control system on aircraft dynamics of flight*, PhD dissertation, Air Force Institute of Technology, Warsaw, Poland, 2008

Copyright Statement

The authors confirm that they, and/or their company or institution, hold copyright on all of the original material included in their paper. They also confirm they have obtained permission, from the copyright holder of any third party material included in their paper, to publish it as part of their paper. The authors grant full permission for the publication and distribution of their paper as part of the ICAS2008 proceedings or as individual off-prints from the proceedings.